Compact in-line temporal measurement of laser pulses with amplitude swing

BENJAMÍN ALONSO,* WAREIN HOLGADO, AND ÍÑIGO J. SOLA

Grupo de Investigación en Aplicaciones del Láser y Fotónica, Departamento de Física Aplicada, University of Salamanca, Salamanca, E-37008, Spain
*b.alonso@usal.es

Abstract: A method of ultrashort laser pulse reconstruction is presented, consisting on the analysis of the nonlinear signal obtained from the interference of the pulse with a replica of itself at a given time delay while varying the relative amplitude between the pulses. The resulting spectral traces are analyzed both analytically and numerically, showing the encoding of the input pulse spectral phase. A reconstruction algorithm is discussed and applied to extract the spectral phase and, jointly to the measured spectral amplitude, reconstructing the pulse. In order to validate the technique, an experimental in-line implementation of the characterization concept is compared to the results from a stablished technique, obtaining a good agreement at different input pulse cases. In sum, a new technique is presented, showing the capability to reconstruct a broad range of temporal pulse durations while its implementation is robust and straightforward, able to be easily adapted to diverse pulse duration and central wavelength ranges.

1. Introduction

The arising of ultrafast optics and the increasing of its applications came in parallel to the need of characterizing the ultrashort laser pulses [1]. As those are turning into increasingly complex and short (to the extreme of single-cycle regime [2,3] or even shorter [4]), the pulse measurements are becoming more and more demanding. The first characterization techniques were based on the pulse autocorrelation [5], obtained from scanning the time delay between two pulse replicas and the measurement of the power of a nonlinear signal depending on the time overlap of both replicas. These methods give an approximate idea of the pulse characteristics but are not able to reconstruct the actual pulse or to provide its spectral phase. Later, the FROG technique [6] used a similar scheme but acquiring the nonlinear signal spectra, instead of the overall nonlinear signal power. The so-called FROG spectrograms, consisting in the nonlinear spectra depending on the replicas delay, encode information of the spectral phase and, by means of reconstruction algorithms [7,8], succeed in reconstructing the pulses. Some years later, the SPIDER technique [9] was invented using spectral interferometry, where both replica remained at a fixed time delay and a spectral shearing was introduced within a nonlinear process. Thus, the derivative of the pulse spectral phase is encoded in the spectral interference of both replicas and extracted by means of Fourier analysis. Another evolution of the spectral interferometry strategy is the self-referenced spectral interferometry (Wizzler) [10], where the reference pulse is cleaned in time, obtaining a flat spectral phase.

A different strategy was presented in 2004 with pulse characterization using phase scanning, the so-called multiphoton intrapulse interference phase scan (MIIPS) [11,12]. The general idea consists in introducing a known set of spectral phases in the test pulse and to observe the second order harmonic generation (SHG) signal of the resulting pulse. The unknown pulse group delay dispersion (GDD) can be therefore extracted at a given wavelength by calculating the amount of GDD within the scan range needed to optimize the SHG signal at that wavelength. Later, the d-scan technique [13] used the spectral phase scan concept with some practical modifications and introduced retrieval algorithms [14–17] to

reconstruct the spectral phase of the test pulse. A related technique was proposed in [18], using an acousto-optic programmable dispersive filter (AOPDF) for the known spectral phase scan and an algorithm to reconstruct both the spectral amplitude and phase of the pulse.

In general, the main part of the time pulse characterization operates under laboratory stability conditions. A major challenge nowadays is to implement characterization set-ups robust and simple enough to work under less controlled conditions. Thus, one of the main goals of the present work is to study the idea and implementation of reconstruction systems capable of facing those demands.

It should be noted that, for designing a characterization set-up, it is needed to take into account the time duration ranges and central wavelength of the pulse to reconstruct, since they are major conditionings for the system implementation. Here, we aimed to develop a simple and robust device for pulse characterization, presenting an in-line configuration, being able to be easily adapted to a broad range of pulse durations.

For this purpose, we explore a different approach of pulse reconstruction technique, consisting on the generation of two pulse replicas at a given time delay, and varying their relative amplitude, thus the term amplitude swing. The resulting time structure is used to generate a nonlinear signal at each case within the range of variation of the pulse replica amplitudes. Then, the nonlinear signal spectrum depending on the pulse relative amplitudes conforms a pattern (i.e., the amplitude swing trace) that, as it will be shown, encodes the spectral phase information, which can be extracted e.g. by applying iterative retrieval algorithms. Firstly, we will devote a section to present and obtain an insight of the technique concept. We will present the theory and an analytical treatment, showing some cases for different GDD and third-order dispersion (TOD) values of the pulses to be characterized, in order to understand more intuitively the physics underneath. Secondly, we will present a reconstruction algorithm for extracting the test pulse information, studying its convergence and errors. Next, one of the possible experimental implementations of the technique will be showed, presenting the experimental results, which will be contrasted with the measurements obtained with an established technique. Finally, the conclusions will be discussed.

2. Amplitude swing concept

Some reconstruction techniques (e.g., autocorrelation, FROG) consist in the time delay scan of two constant amplitude replicas (it can be done either in collinear or non-collinear configurations) and the generation, at each time delay, of a nonlinear signal yield from the interaction of the resulting time amplitude overlapped distribution with a nonlinear medium. Typically, the creation of the two replicas and the time delay scan is performed by using an interferometer, what makes the set-up sensitive to noise, although several alternate and more compact configurations have been proposed [19–21]. The SPIDER technique, on the other hand, uses spectral interferometry with a fixed delay between the replicas and techniques such as MIIPS and d-scan do not use pulse replicas, being more stable because of their in-line configuration.

In this work we propose a different approach for the pulse reconstruction by using two pulse replicas shifted by a given temporal delay and varying their relative amplitude before a nonlinear process. The temporal delay can be chosen in such a way that the two replicas can overlap on time. By varying their relative amplitude, the pulse replica interference in the time domain results in a modulation of the evolution of the temporal amplitude and phase of the interference pulse. If subsequently the resulting pulse generates a nonlinear signal (e.g., second harmonic generation, SHG), the nonlinear spectrum will strongly depend on its time evolution, which at the same time depends on the phase of the input pulse. Therefore, by scanning the amplitude balance between the two replicas the spectrum of the nonlinear signal may change, encoding information about the original input pulse. We refer to the technique as amplitude swing.

In the implementation that we present in this work (depicted in Fig. 1a), the input pulse to be measured has horizontal (x-axis) linear polarization. This pulse propagates through a multiple-order wave-plate (MWP) in normal incidence, where the propagation axis is chosen to be z. For this first analysis, we consider that the MWP operates as a half-wave plate for the central wavelength. When the fast axis of the MWP is oriented at different angles θ with respect to the x-axis, then the input pulse is projected onto the fast and slow axes of the MWP with different amplitudes. Due to the birefringence of the MWP, these projections are delayed in time. After the MWP, a horizontal linear polarizer (LP) projects again the two pulse replicas onto the x-axis, with the amplitude of each replica depending on θ. The first replica (fast axis) is firstly projected from the x-axis to the fast axis of the MWP, and secondly from the fast axis to the x-axis in the LP, therefore its amplitude is modulated by $\cos^2\theta$. The second replica is projected in a similar way but to the slow axes, thus its amplitude being modulated by $\sin^2\theta$. By rotating the MWP, the different relative amplitudes range continuously from having a single replica if $\theta = m\pi/2$ (either the first or the second one) to having equal amplitudes if $\theta = (2m+1)\pi/4$.

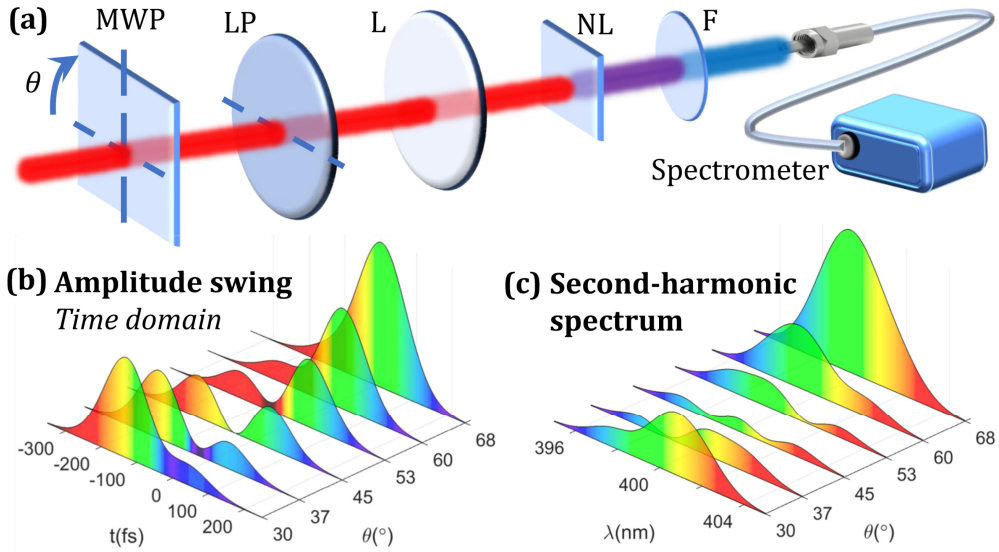

Fig. 1. (a) Scheme of the experimental implementation: the input beam with horizontal linear polarization passes through a multiple-order wave-plate (MWP) that can rotate at angles θ; then, a linear polarizer (PL) selects one polarization projection (e.g., horizontal polarization); a lens (L) focused the beam onto a nonlinear material (NL), in our case a 20-μm thickness BBO crystal; finally, the resulting nonlinear signal is analyzed by means of an spectrometer, where the fundamental is filtered out with F. For an example of positively chirped input pulse, (b) the temporal intensity of the two interfering fundamental replicas and (c) their second-harmonic generation spectrum are represented for a selection of relative amplitudes due to different rotation angles θ. In (b), the temporal intensity is colored with the instantaneous wavelength (the color scale is the same than the corresponding second-harmonic in (c)).

In Fig. 1b, we show an example of the effect of the amplitude swing on the fundamental pulse (after the LP), when the input pulse has positive linear chirp (corresponding to the case presented before in Fig. 2 with GDD=+5000 fs^2), for a selection of angles θ close to the amplitude balance (45°), the first replica is centered in t=−100 fs and the second replica is centered in t=0 fs. The interference pulse intensity is colored with the calculated instantaneous wavelength in the pulse. For the angle θ=68°, the tendency is that the second replica is dominating, showing a gaussian temporal profile and a constant linear chirp (except for the pre-pulse tail where there is still interference with the first replica). For other angles

closer to θ=45°, there is a temporal destructive or constructive interference depending on the spectral phase of the input pulse. By observing the instantaneous wavelength, it is seen that the interference pulse does not have a pure linear chirp anymore, thus we conclude that the temporal amplitude and phase are both varying when the amplitude swing in performed. If this signal experiments a nonlinear process, for example SHG in a nonlinear (NL) crystal, then the resulting spectrally-resolved signal encodes the pulse information [22], thus allowing the pulse characterization. In Fig. 1c, we represented the SHG spectrum of the previously described case, where the spectral content for the different angles θ is directly related to the temporal interference shown in Fig. 1b. For example, for angles θ>45°, the bluish part of the spectrum is dominating, while for θ<45° the reddish part of the spectrum has more signal. Thus, a gate in the pulse amplitude can be observed in the front or rear part of the pulse. The result would be the opposite in the case of negative GDD and the modulation of the interferences is a fingerprint of the magnitude of the GDD. We will get back to this analysis in more depth when describing the simulations with a pure GDD.

For the sake of clarity and to obtain a theoretical insight into the proposed strategy, as described before we consider the particular case of an input pulse linearly polarized on the horizontal (x-) axis with normal incidence onto the MWP. This MWP introduces a certain optical path difference $\delta(\omega)=\Delta n(\omega)\cdot d$, where $\Delta n(\omega)=n_y(\omega)-n_x(\omega)$ is the material birefringence between two orthogonal projections, and d is the thickness of the MWP. Therefore, when the linearly polarized pulse propagates through the MWP, its electric field vector is decomposed into the projection on the fast and slow MWP axes with a dephase (and thus, a time delay) depending on δ(ω). After passing through the MWP oriented at θ, the field amplitude in x- and y-axis will be

$$E_x(\omega) = E_0(\omega)(\cos^2\theta + e^{i\frac{\delta(\omega)\cdot\omega}{c}}\sin^2\theta) \tag{1}$$

$$E_y(\omega) = E_0(\omega)(1 - e^{i\frac{\delta(\omega)\cdot\omega}{c}})\cos\theta\sin\theta \tag{2}$$

where $E_0(\omega)$ is the input pulse complex amplitude. For simplicity in the discussion of the technique concept, we disregard in this theoretical analysis the dispersion of the fast axis, but it is taken into account in the retrieval algorithm.

Then, we consider the horizontal component after the MWP, i.e. $E_x(\omega)$, which can be obtained experimentally by using a linear polarizer oriented along the x-axis. According to Eq. (1), the resulting field will be composed by two replicas, whose relative amplitudes depend on θ and their relative dephase and delay depends on $\delta(\omega)$. Just by Fourier transforming $E_x(\omega)$, the time domain evolution can be worked out [Eq. (3)]

$$E_x(\mathrm{t}) = \frac{1}{2\pi}\int E_0(\omega)(\cos^2\theta + e^{i\frac{\delta(\omega)\cdot\omega}{c}}\sin^2\theta)e^{i\omega t}d\omega \tag{3}$$

Then, the SHG signal of this field will be

$$E_x^{SHG}(\omega) = \int [E_x(\mathrm{t})]^2 e^{-i\omega t}dt \tag{4}$$

And therefore, the final SHG spectrum will be proportional to

$$S_x^{SHG}(\omega) = \left|E_x^{SHG}(\omega)\right|^2 = \left|\int [E_x(\mathrm{t})]^2 e^{-i\omega t}dt\right|^2 \tag{5}$$

In order to obtain analytical expressions for understanding the process, it is considered a test pulse amplitude being $E_0(\omega) = A_0\, \mathrm{e}^{-i\cdot b(\omega-\omega_0)^2}\mathrm{e}^{-(\omega-\omega_0)^2/\Gamma^2}$ with Gaussian spectral amplitude (bandwidth Γ), central wavelength ω_0 and with quadratic spectral phase given by b (note that $b = GDD/2$). For the sake of simplicity, we consider $\delta(\omega)$ to be constant along the pulse spectral components, that is $\delta(\omega) = \delta$. This is a good approximation in the present work since, e.g. for α–quartz, $\delta(\omega) = 0.0089$ in the spectral region ranging from 700 nm to 850 nm [23]. Thus, both replicas present a constant time delay $\tau = \delta/c$.

Then, applying Eq. (3), the time domain distribution will be

$$E_x(t) = \frac{A_0}{\sqrt{2}\sqrt{\Gamma^{-2}+ib}}\left(e^{-i\omega_0 t-\frac{1}{1+ib\Gamma^2}\left(\frac{t\Gamma}{2}\right)^2}\cos^2\theta + e^{-i\omega_0\left(t-\frac{\delta}{c}\right)-\frac{1}{1+ib\Gamma^2}\left(\left(t-\frac{\delta}{c}\right)\frac{\Gamma}{2}\right)^2}\sin^2\theta \right) \tag{6}$$

Applying the result of Eq. (4) to Eq. (6), the SHG field will be

$$E_x^{SHG}(\omega) = \frac{A_0^2 e^{-\left(1+ib\Gamma^2\right)(\omega-2\omega_0)^2/2\Gamma^2}}{\sqrt{\Gamma^{-2}+ib}}\left(\frac{\cos^4\theta}{2} + e^{-\frac{1}{2\left(1+ib\Gamma^2\right)}\left(\omega\frac{\delta}{c}+\left(\frac{\Gamma\delta}{2c}\right)^2\right)}\cos^2\theta\sin^2\theta + \frac{e^{i\omega\frac{\delta}{c}}\sin^4\theta}{2} \right) \tag{7}$$

whose dependence has a global factor and three terms. The first term is related to the SHG of the first replica (fast axis), the last term to the SHG of the second replica (slow axis) and the middle term is the SHG of the crossed term of the first and second replicas. I SHG spectrum can be calculated as $S_x^{SHG} = \left(E_x^{SHG}\right)^* E_x^{SHG}$, giving

$$\begin{aligned} S_x^{SHG}(\omega,\theta) = {} & \frac{A_0^4 e^{-2(\omega-2\omega_0)^2/2\Gamma^2}}{4\sqrt{\Gamma^{-4}+b^2}}\times \\ & \left\{ \cos^8\theta + 4e^{-\frac{1}{2\left(1+b^2\Gamma^4\right)}\left(\frac{\Gamma\delta}{2c}\right)^2}\cos\left[\frac{\omega}{2}\frac{\delta}{c}+\frac{b\Gamma^4}{8\left(1+b^2\Gamma^4\right)}\left(\frac{\delta}{c}\right)^2\right]\cos^6\theta\sin^2\theta \right. \\ & + 2\cos\left(\omega\frac{\delta}{c}\right)\cos^4\theta\sin^4\theta + 4e^{-\frac{1}{\left(1+b^2\Gamma^4\right)}\left(\frac{\Gamma\delta}{2c}\right)^2}\cos^4\theta\sin^4\theta \\ & \left. + 4e^{-\frac{1}{2\left(1+b^2\Gamma^4\right)}\left(\frac{\Gamma\delta}{2c}\right)^2}\cos\left[\frac{\omega}{2}\frac{\delta}{c}-\frac{b\Gamma^4}{8\left(1+b^2\Gamma^4\right)}\left(\frac{\delta}{c}\right)^2\right]\cos^2\theta\sin^6\theta + \sin^8\theta \right\} \end{aligned} \tag{8}$$

Therefore, the SHG spectrum depends on b (i.e., $2\cdot GDD$), so the $S_x^{SHG}(\omega,\theta)$ trace encodes the information concerning the spectral phase (the quadratic component in this simplified case). The main dependence on the pulse phase is encoded in the two cosine terms depending on b. By comparison with Eq. (7), it is deduced that those terms actually correspond to the spectral interference between the crossed SHG described before and the SHG of each individual replica. Note that from Eq. (8) it is possible to have an intuitive idea of the appropriate time delay (i.e., value of $\tau = \delta/c$) for optimizing the $S_x^{SHG}(\omega,\theta)$ trace sensitivity to the pulse chirp. For instance, let us consider high δ values (i.e., a high difference of optical length between the ordinary and extraordinary components). Since all the cosine

terms with dependence on b are linked to a negative exponential depending on δ, the higher is δ, the smaller are the terms depending on b (except the global scale term), so the phase information is lost or, at least, very much faded. On the other hand, the smaller is δ, the less sensitive is the $S_x^{SHG}(\omega,\theta)$ trace to b due to the cosine tending to 1. Notice that the optimal value of δ is also linked to the spectral bandwidth Γ: the smaller Γ is, the larger should be δ in order to maintain the negative exponential and the cosine arguments. As a trade-off, we find that it is a good choice a temporal delay τ of the order of the Fourier-limited pulse duration, independently on the possibly longer actual pulse duration due to chirp. This criterion is flexible, we have checked that the pulse is correctly reconstructed using an MWP that introduces a delay 0.5 and 2 times the Fourier-limit FWHM.

Fig. 2 shows, for different input pulse GDD values (columns), the fundamental pulse intensities (row 1, a-e) and the simulated SHG spectra depending on the MWP angle (row 2, f-j), and the corresponding retrievals (row 3, k-o), when a half-wave MWP designed for operation at 800 nm is to be considered (note that the trace retrievals will be discussed in the next section, but we include them here to better compare the simulated and retrieved traces). We use a Gaussian spectrum centered at 800 nm with a Fourier-limit of 100 fs at full-width at half maximum (FWHM). Notice that the SHG traces in Fig. 2 have been individually normalized, as usual in characterization techniques. As previously discussed, the amplitude swing trace depends on the optical path difference δ between the slow and fast components of the MWP, and it is convenient to choose a value of δ neither too high nor too low. As discussed before, here we select a temporal delay $\tau = \delta/c$ equal to the FWHM of the Fourier-transform-limited pulse.

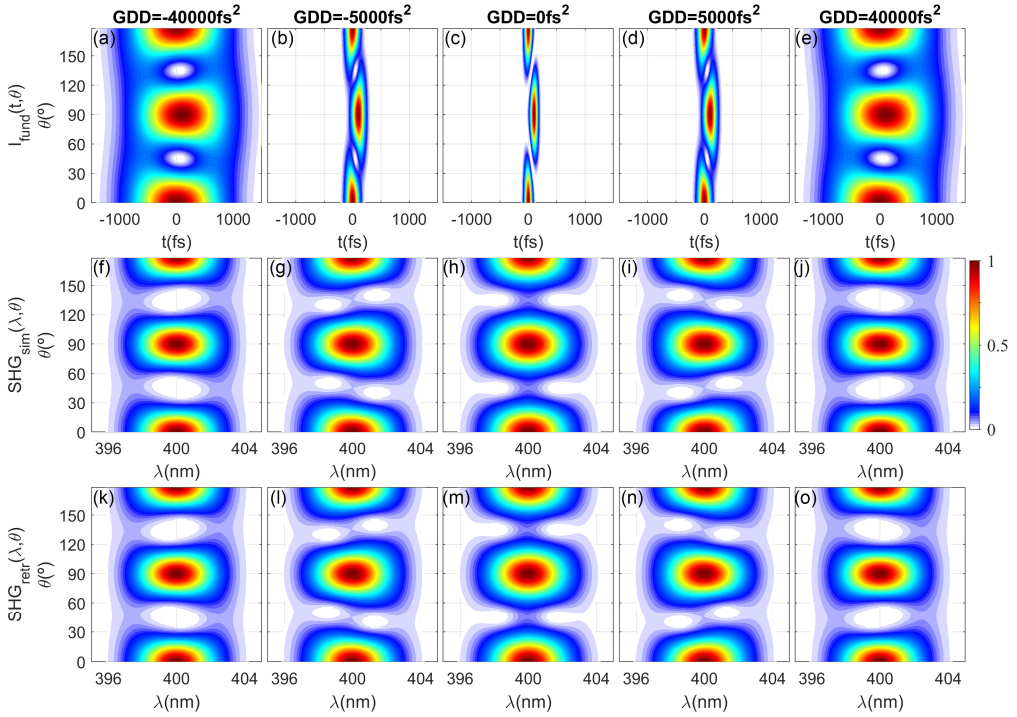

Fig. 2. Temporal intensity of the two replicas of the input pulse (linearly polarized on the x-axis) after the MWP and a linear polarizer oriented along the x-axis, depending on the angle θ between the MWP fast axis and the input pulse polarization direction, also along the x-axis (row 1), and corresponding simulated (row 2) and retrieved (row 3) amplitude swing traces of the SHG of the resulting pulses. Different GDD values are represented in the

columns, GDD= -40000 fs^2, -5000 fs^2, 0 fs^2, +5000 fs^2, +40000 fs^2, respectively. The traces are individually normalized.

For those simulations we have used the numerical calculations. The results would be the same if the analytical expressions derived above were applied, as they are exact under the considered assumptions, for which we have checked that the analytical and numerical traces are identical.

Fig. 2c shows the time evolution of the pulses after the MWP and a linear polarizer oriented along the x-axis, depending on the angle θ between the MWP fast axis and the input pulse polarization direction (along the x-axis), when the input pulse is Fourier limited. Because of the selection of δ, the fast and slow pulse projections are close, but they barely interfere on the time domain. The resulting $S_x^{SHG}(\omega,\theta)$ trace (Fig. 2h) registers the spectral distribution of the two resulting SHG pulses depending on their relative amplitude. If a non-zero GDD is considered, e.g. GDD=+5000 fs^2, the input pulse broadens in time, exhibiting the lower (reddish) frequencies in the front part of the pulse and the higher (bluish) frequencies in the rear one (or contrarily if the GDD is negative). As a result, the two replicas interfere in the time domain (Fig. 2d). This interference depends on the MWP rotation angle (i.e., the relative amplitude between the replicas), as seen for the present case in Fig. 1b for a selection of angles close to the amplitude balance. Therefore, the $S_x^{SHG}(\omega,\theta)$ trace changes (Fig. 2i), exhibiting a dependence on the GDD, due to the fact that the trace encodes the spectral phase. In the particular cases of rotation angles θ=0º, 90º and 180º, the SHG spectrum (Fig. 2, row 2) is generated by a single pulse (Fig. 2d), being either the slow or the fast component, since one pulse of the replicas has zero amplitude. At angles around θ=30º and 150º, the first pulse (fast axis) of the two replica has higher amplitude than the rear one (slow axis) (Fig. 2d). Therefore, its reddish components (since we are now considering positive GDD, they are located at the front of the pulse) will prevail in the resulting interference, as observed in the corresponding SHG spectra (Fig. 2i) (see also in Fig. 1b and 1c). Conversely, at angles around θ=60º and 120º, the rear pulse will be predominant in the interference (Fig. 2d). Thus, its bluish part (i.e., the rear part of the pulse) will prevail, imprinting a bluish signal in the SHG spectra (Fig. 2i) (see also in Fig. 1b and 1c). In the cases of equal amplitudes of the replicas (θ=45º and 135º), after the interference only the leading part of the first pulse and the trailing part of the second one are observed. For low GDD input pulse cases, the spectra of both resulting parts may present a certain spectral overlap, arising the spectral peak at the center of the SHG spectra (Fig. 2i). This is also seen for θ=45º in Fig. 1b and 1c, where the SHG of the two delayed replicas (reddish and bluish, respectively) corresponds to a reddish and bluish signal together with the crossed term peaked at the central wavelength. However, when the input pulse GDD is high enough, the two peaks from the interference (Fig. 2e) will not exhibit any spectral overlap (Fig. 2j): in the considered positive GDD case, the first pulse will show low frequency components and the second one, high frequency components. Thus, the central frequency peak at the SHG spectra will disappear, while the red shift (θ= 30º and 150º) and blue shift (θ=60º and 120º) regions are still observed, but in a smoother way. When considering negative GDD of the pulse (columns 1 and 2), a similar reasoning applies except for the opposite temporal chirp of the replicas, therefore being translated into the SHG trace in a similar way but exchanging the blue and red terms above.

Thus, the amplitude swing traces, $S_x^{SHG}(\omega,\theta)$, show some features coming from spectral interference and optical gating, depending on the input pulse characteristics. In the commented examples, the amount of GDD can be estimated intuitively: when the GDD is very low (e.g., in the Fig. 2 example, GDD= 0 fs^2), the expected spectral interference of two pulses close but not overlapping in time appears (in the example, around 400 nm at θ=45º and 135º); for intermediate GDD (e.g., in the Fig. 2 example, GDD=±5000 fs^2), that feature

remains at θ=45º and 135º, pointing out that there is still spectral overlapping, while the shift of the SHG spectrum at θ=30º and 150º gives an idea of the sign of the GDD. Finally, for high values of GDD (e.g., in the Fig. 2 example, GDD=±40000 fs^2) the central interference disappears as previously commented.

As previously commented, the selection of the time delay $\tau = \delta/c$ is important and linked to the pulse spectral bandwidth. If τ is much higher than the FL pulse duration, within the whole range of GDD values where there is not temporal overlap between the two replicas there will not be information from the spectral phase. On the other hand, if τ is much lower than the FL duration, the two replicas will interfere destructively almost entirely in the angles corresponding to similar replica amplitudes, so no information could be extracted. In sum, the value of τ must be around the Fourier-limit pulse duration, which is known from the pulse spectrum. To adapt the technique to pulses exhibiting different spectral bands and pulse duration ranges, it is necessary to adjust τ consequently (i.e., by changing the MWP by another with the correct thickness or by using a pair of birefringent wedges and adjusting their insertion), whenever the nonlinear material shows correct phase matching and the spectrometer resolves the SHG signal.

The features of the traces in Fig. 2 come from considering a MWP acting as a half-wave at the central frequency. If the phase retardation of the MWP were different, the amplitude swing trace structure would change, exhibiting the minima and maxima at different frequencies. Nevertheless, the phase information is still encoded and can be extracted using reconstruction algorithms, as discussed in Section 3 and shown experimentally in Section 4.

The effect of the TOD has also been numerically studied (Fig. 3), considering the same spectrum (100 fs FWHM Fourier limited centered at 800 nm) and MWP (half-wave at 800 nm, introducing a delay of 100 fs) than in the previous case. The pulse TOD values range from $-4\cdot10^6$ fs^3 to $+4\cdot10^6$ fs^3.

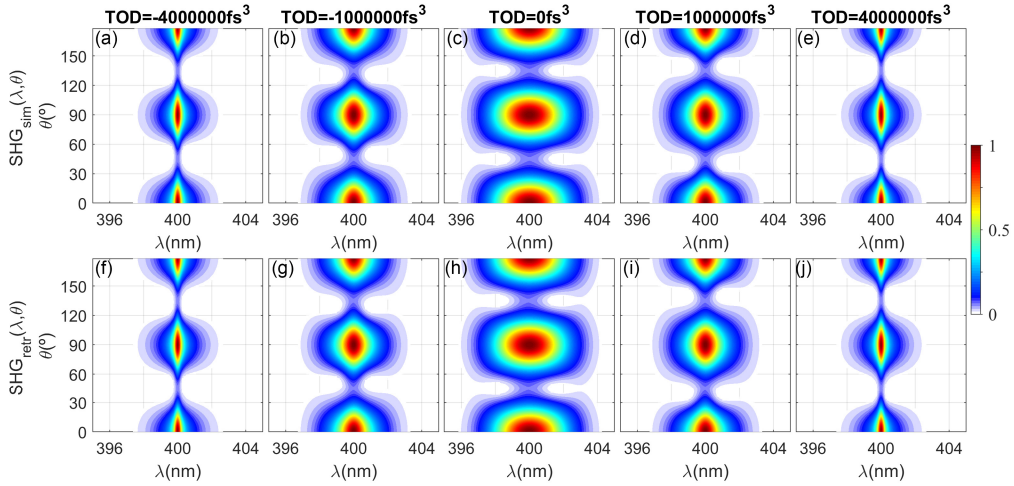

Fig. 3. Simulated (row 1) and retrieved (row 2) amplitude swing traces depending on the angle θ. Different TODs are represented in the columns, TOD= −4000000 fs^3, −1000000 fs^3, 0 fs^3, +1000000 fs^3, +4000000 fs^3, respectively. The traces are individually normalized.

Here, the TOD is manifested in the $S_x^{SHG}(\omega,\theta)$ traces through a contraction of the trace in the spectral dimension. The higher the module of the TOD is, the sharper is the figure in the abscise axis. Also, this can be interpreted through the stretching of the minima in the angle θ dimension. The sign of the TOD is also manifested, mainly in the location and width of those minima. In Fig. 3b (TOD=−1000000 fs^3), for angles around θ=45º (θ=135º) the minima region, is slightly shifted towards higher (lower) angles, contrarily to what happens in

Fig. 3d (TOD=+1000000 fs^3). For higher values of the module of the TOD (e.g., Fig. 3a and Fig. 3e), the tendency is the same but the difference in the minima locations becomes less perceptible, still distinguishable by the eye if superimposing the traces. Actually, the difference between those traces (Fig. 3a and 3e) reaches 3% with respect to the maximum of the trace. Furthermore, as we will see in the next section, the algorithm is able to discriminate both cases for the high TOD values considered in the examples.

In order to test the technique sensitivity for those high TODs, we have added 1% white noise (noise to signal ratio) to the simulated trace with TOD=+4000000 fs^3 (Fig. 4a), correctly reconstructing the trace (Fig. 4b). It should be noticed that the similarity of the traces in Fig. 3a and 3e only arises when the chirp value is very high (either changing the sign in GDD, TOD or arbitrary chirp), the spectral amplitude of the pulse is symmetrical and the phase retardation introduced by the MWP is exactly (2m+1)π for the central wavelength (half-wave plate operation). For example, if the MWP introduces a retardation of 0.8π, the simulated traces for that value of TOD, positive (Fig. 4c) and negative (Fig. 4d), become distinguishable in the regions of the traces where the replicas interfere with comparable amplitudes. A similar conclusion is obtained when the spectral amplitude is not perfectly symmetrical, for example by adding a slight spectral tail. Therefore, in a realistic case, it is unusual simultaneously fulfilling all the conditions for the similarity (symmetrical spectral amplitude, half-wave operation for the central wavelength and very high chirp) and, even in that case and with a noisy trace, the pulse could be reconstructed. The discussed cases conform the limits of the technique for the present pulse spectrum (in the symmetric case) and the noise is below the difference between the two traces for opposite sign phase. We have found that the range of measurable GDDs and TODs is large, as we will further experimentally confirm in Section 4.

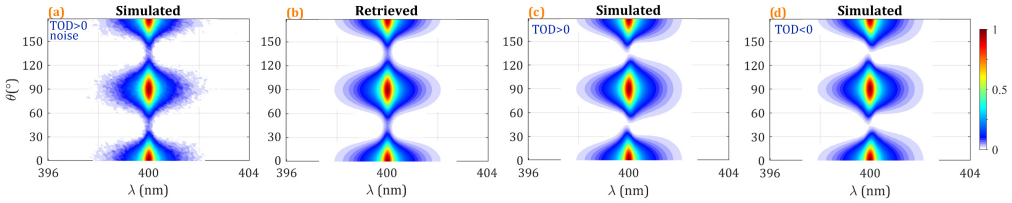

Fig. 4. Simulations for the higher value TOD=±4000000 fs^3. (a) Simulated amplitude swing trace for TOD>0 and (b) the corresponding retrieved trace. Comparison of the simulated trace for (c) TOD>0 and (d) TOD<0 when the MWP has 0.8π (+2πm) phase retardation for the central wavelength.

3. Reconstruction algorithm

We define the electric field of the pulse to be measured as $E(\omega) = A(\omega)\mathrm{e}^{i\varphi(\omega)}$, where its amplitude is calculated from the measured power spectrum, $S(\omega)$, as $A(\omega) = \sqrt{S(\omega)}$. The spectral phase $\varphi(\omega)$ is encoded in the two-dimensional SHG amplitude swing trace, which is given by

$$S_x^{SHG}(\omega,\theta) = \left| \int \left(\int A(\omega')\mathrm{e}^{i\varphi(\omega')} \left[\mathrm{e}^{i\rho_f(\omega')} \cos^2\theta + \mathrm{e}^{i\rho_s(\omega')} \sin^2\theta \right] \mathrm{e}^{i\omega' t}\, d\omega' \right)^2 \mathrm{e}^{-i\omega t}\, dt \right|^2 \qquad (9)$$

At this point, we consider the general case of a birefringent plate with the fast axis oriented at an angle θ with respect to the linear polarization of the input pulse (horizontal), with the spectral phases introduced by the fast and slow axes, respectively $\rho_f(\omega)$ and $\rho_s(\omega)$. Those phases can be calculated from the ordinary and extraordinary refractive indices of the MWP from their Sellmeier equations [23], provided that the thickness is known. The relative phase of the plate axes may be known if the phase retardation is given by the manufacturer or can be calibrated, as we do in the experiments (e.g., using the technique described in [24]). As

described in Section 2, the expression in Eq. (9) accounts for the input pulse propagation through the MWP followed by the horizontal linear polarizer (LP). The sum of the terms $e^{i\rho_f(\omega')}\cos^2\theta$ and $e^{i\rho_s(\omega')}\sin^2\theta$ corresponds to the projection for different orientations θ of the input pulse (x-axis) onto the fast and slow axes, respectively, and then to the x-axis with the LP. Then, it is calculated the SHG signal (modeled as the square of the pulse in the temporal domain) and finally the spectral detection of the signal.

In Eq. (9), all quantities are known, except for the pulse phase. We use a guess phase to calculate a first retrieved trace, and then we use the measured trace to be compared with the retrieved trace for the current spectral phase of the pulse, $\varphi(\omega)$. To do this, we define a merit function, calculating the dissimilarity between the experimental and the retrieved trace as the square of the difference between their amplitudes. By minimizing the merit function, the phase is iteratively modified until the retrieved trace converges to the experimental trace. We can parametrize the phase function in different ways, for example as a Taylor series, Fourier series, direct discretization and interpolation of the phase, or combinations of them [13,14,16,25]. We deal with the problem as a multi-variable optimization in which the phase parametrization is the unknown. This kind of problem has already been solved e.g. with d-scan retrievals, using different algorithms, for example non-linear optimization with Nelder-Mead Simplex [13], projections [15], or differential evolution [17]. We choose to perform the phase retrievals with the Levenberg-Marquardt algorithm, which has been previously shown to be robust performing retrievals of d-scan [3,16,26] as well as other techniques [27]. The guess spectral phase is arbitrary, it can be kept e.g. to a flat phase or to a random phase. We firstly run a fast optimization with a Taylor expansion of the phase up to order 10 and then we use the output as a seed for a subsequent optimization, in which we optimize the derivative of the spectral phase in 32 points, while interpolating in the rest of the frequency sampling.

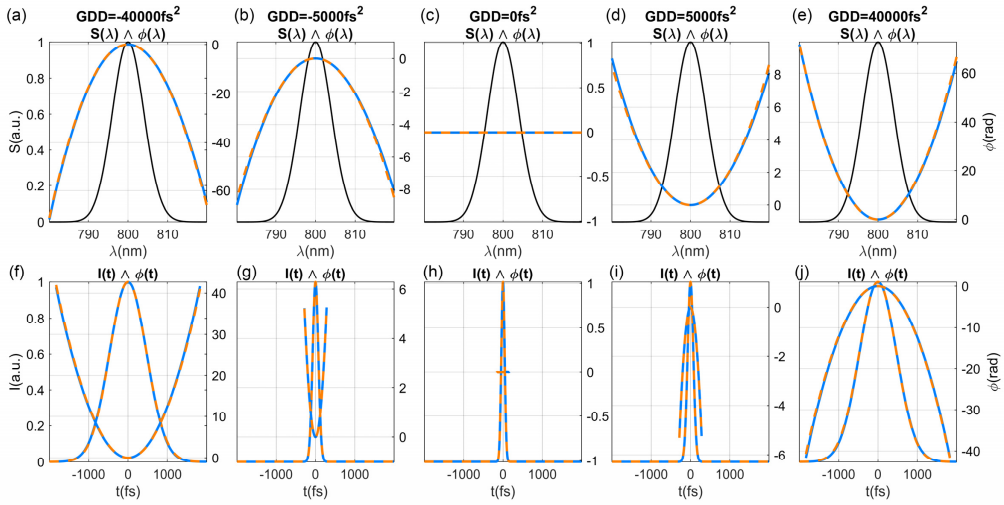

Fig. 5. Row 1: Simulated spectrum (black) and phase (solid blue); retrieved spectral phase (dashed red). Row 2: Simulated (solid blue) and retrieved (dashed red) temporal intensity and phase. Different GDDs are represented in the columns, GDD= −40000 fs^2, −5000 fs^2, 0 fs^2, +5000 fs^2, +40000 fs^2, respectively.

Fig. 5 presents the pulse retrievals corresponding to the retrieved $S_x^{SHG}(\omega,\theta)$ traces at different input GDD cases (Fig. 2, third row). Fig. 5, row 1 shows the spectral amplitude (black curve), the simulated experimental spectral phase (blue curve) and the reconstructed spectral phase (red curve) for GDD values of −40000 fs^2 (Fig. 5a), −5000 fs^2 (Fig. 5b), 0 fs^2 (Fig. 5c), +5000 fs^2 (Fig. 5d) and +40000 fs^2 (Fig. 5e), corresponding to the simulations

presented in Fig. 2. The retrieved traces are shown in Fig. 2k-o (compared to the simulated traces in Fig. 2f-j), respectively. The agreement between the expected and retrieved spectral phases is good. Consequently, the time domain retrieved pulses (Fig. 5f-5j; red curve) also exhibit a good agreement with the simulated (blue curve) at both the pulse intensity and phase, spanning cases from Fourier-limited pulse duration (100 fs) to around 1 ps (FWHM) characterized by the same set-up.

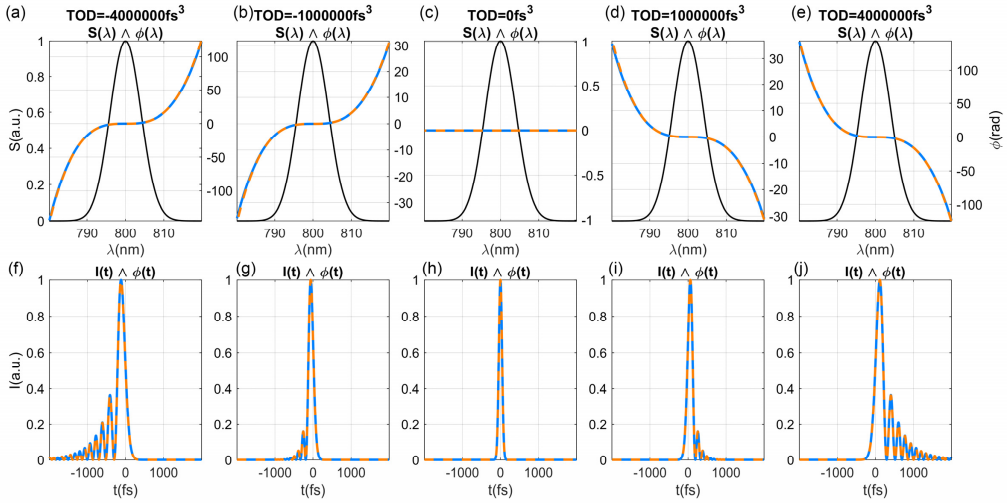

Fig. 6. Row 1: Simulated spectrum (black) and phase (solid blue); retrieved spectral phase (dashed red). Row 2: Simulated (solid blue) and retrieved (dashed red) temporal intensity. Different TODs are represented in the columns, TOD= −4000000 fs^3, −1000000 fs^3, 0 fs^3, +1000000 fs^3, +4000000 fs^3, respectively.

Similarly, Fig. 6 presents the pulse reconstructions corresponding to the retrieved $S_x^{SHG}(\omega,\theta)$ traces at different input TOD cases (Fig. 3f-j), which shows a good convergence to the simulated traces (Fig. 3a-e). Fig. 6, row 1 shows the spectral amplitude (black curve), the simulated experimental spectral phase (blue curve) and the reconstructed spectral phase (red curve) for TOD values of −4000000 fs^3 (Fig. 6a), −1000000 fs^3 (Fig. 6b), 0 fs^3 (Fig. 6c), +1000000 fs^3 (Fig. 6d) and +4000000 fs^3 (Fig. 6e), corresponding to Fig. 3f-j, respectively. In the time domain (Fig. 6f-6j), the retrieved time intensities (red line) are compared to the simulated ones (blue curve). Again, the simulated and reconstructed pulses match very well in both the spectral and time domains. The technique is able to retrieve pulses with pre- or post-pulse structure spanning around 2 ps in the temporal domain. Note that the retrievals shown in Fig. 2,3,5,6 for different GDD and TOD values have been all obtained considering the same set-up characteristics (i.e., the same MWP introducing a fixed delay τ).

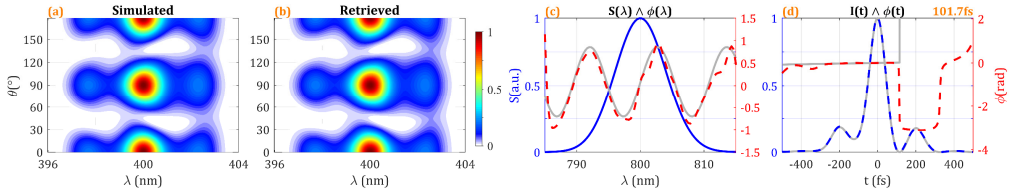

Fig. 7. Simulation of a moderate oscillatory spectral phase. (a) Simulated and (b) retrieved amplitude swing traces. (c) Spectrum (blue) and retrieved spectral phase (dashed red). (d) Retrieved temporal intensity (dashed blue) and phase (dashed red). Gray curves in (c) and (d) correspond to the simulated magnitudes for comparison.

In this section, we have studied the effect of different amounts of GDD and TOD ranging from zero to high absolute values (positive and negative). We have also simulated more moderate spectral phase variations for GDD=+300 fs^2 and GDD=+600 fs^2, corresponding to phase variations below 0.5 rad, finding that the reconstruction retrieves those phases and the pulse duration with precision. As an example, we show here the simulation of an oscillating spectral phase (amplitude of the oscillation 0.25π) for an MWP operating as 0.4λ retarder for the central wavelength (Fig. 7a). The reconstructed amplitude swing trace converges correctly (Fig. 7b), and the spectral phase retrieved and the temporal intensity and phase (Fig. 7c and 7d) agree with the simulated input pulse.

4. Experimental set-up and results

The implementation of the technique was presented in Fig. 1a. The incoming beam (central wavelength at 797 nm, 10 nm spectral FWHM, 84-fs Fourier-limit duration), from a chirped pulse amplification (CPA) laser system (Spitfire from Spectra Physics), presenting a horizontal (X) linear polarization, passes through a 3-mm quartz MWP, mounted in a rotating motor and used to split the test pulse into the two replicas and to change their relative amplitudes as the angle θ is varied. The MWP introduces a delay of 95 fs between the fast and slow axes pulse projections and behaves as half-wave plate at 800.5 nm. The phase retardation introduced for the central wavelength (797 nm) is 0.69π, differing from half-wave operation. Notice that in the theoretical analysis we used a dephase of π for the central wavelength as an example and, as said in the Section 2, it is not a requirement. After that, a linear polarizer (LP) selects the horizontal component of the polarization. The beam is then focused by means of a lens (L) onto a BBO type I crystal (NL, 20-μm thickness guaranteeing the phase matching for the beam bandwidth). The remaining fundamental radiation is filtered out with a linear polarizer (F). The SHG radiation is collected by means of an optical fiber connected to a spectrometer (HR4000, Ocean Optics Inc.). The measurement process consists in controlling the rotation stage position θ and acquiring the corresponding spectrum. The dispersion of the diverse elements (MWP, LP and L) is taken into account within the reconstruction algorithm so that it does not affect the obtained spectral phase. The spectrum of the fundamental pulse was recorded by a spectrometer (AvaSpec 2048-USB1, Avantes Inc.).

In order to study the validity of the proposed approach, the experimental results of the amplitude swing technique have been compared to those obtained applying an established technique, in our case the d-scan technique (already compared to FROG [28] and SPIDER [29]) in its self-calibrating version [16]. To that purpose, we have used the internal CPA grating compressor to perform the dispersion scan with the same 20-μm thickness BBO crystal. The SHG spectra for 118 positions (different values of the grating distance using a constant step between consecutive positions) of the laser compressor are measured with the spectrometer (HR4000, Ocean Optics Inc.). Fig. 8a shows the experimental d-scan trace. The linear tilt of the d-scan trace is an indicator of the optimally compressed pulses presenting an almost pure positive TOD leading to post-pulses. As discussed in [16], the self-calibrating d-scan algorithm is able to simultaneously reconstruct the test pulse and the unknown dispersion introduced during the scan. Fig. 8b shows the retrieved d-scan trace obtained by applying the self-calibrating algorithm and Fig. 8c presents the experimental pulse spectrum used both for the d-scan and amplitude swing retrievals. The dispersion axis in Fig. 8a and 8b corresponds to the retrieved GDD introduced by the compressor, considering the zero dispersion the position of maximum SHG signal. The dashed lines in Fig. 8a indicate the CPA compressor grating positions (A-D) where the comparison between both techniques was performed. The different cases, from A to D (scan positions 54, 63, 68, and 75, respectively), correspond to adding positive dispersion, i.e., to reduce the gratings distance. From the self-

calibrating d-scan retrieval we calibrate the dispersion per step imparted by the compressor, which is GDD=+1685 fs^2 and TOD=−14390 fs^3.

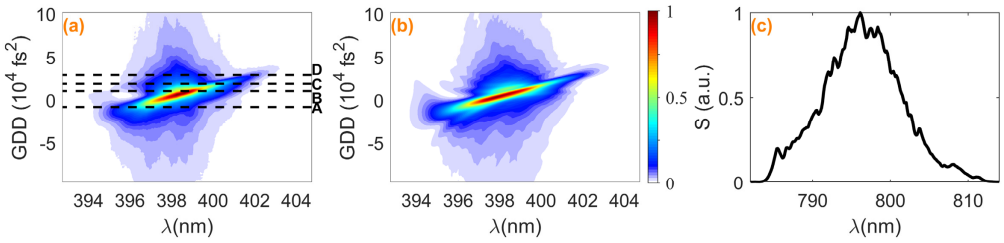

Fig. 8. (a) Experimental and (b) retrieved d-scan trace. (c) Experimental pulse spectrum used both for the d-scan and the amplitude swing retrievals shown in Fig. 9.

Fig. 9 presents the amplitude swing results at those diverse cases of compression of the input pulses (rows A-D). The experimental amplitude swing traces for the different compressor positions are presented in the first column of Fig. 9, observing a clear change in the $S_x^{SHG}(\omega,\theta)$ traces from one case to another. The corresponding retrieved $S_x^{SHG}(\omega,\theta)$ traces are shown in the second column of Fig. 9, observing good matching with the corresponding experimental ones.

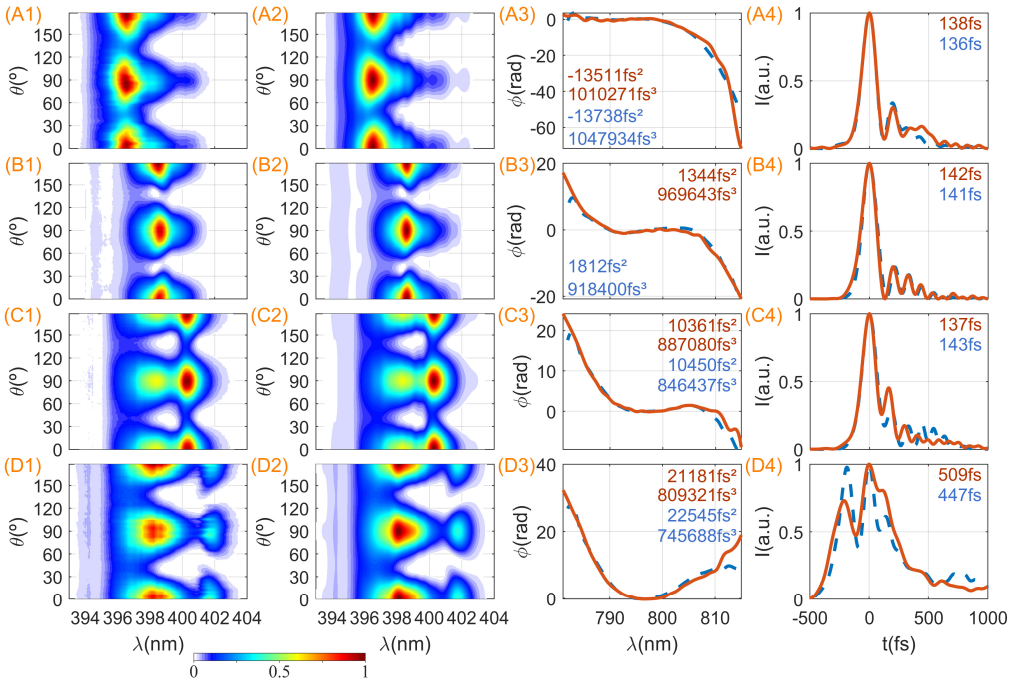

Fig. 9. Experimental amplitude swing traces (column 1); corresponding retrieved traces (column 2). The retrieved spectral phases (column 3, solid red curve) and time domain pulse intensities (column 4, solid red curve) with amplitude swing are compared to the corresponding retrieved spectral phases (column 3, dashed blue curve) and time domain pulse intensities (column 4, dashed blue curve) from the self-calibrating d-scan. In column 3, the calculated GDD and TOD values from the spectral phase are given for the amplitude swing (red) and for the d-scan (blue). In column 4, the measured pulse duration (FWHM) is given for the amplitude swing (red) and for the d-scan (blue). Rows A-D correspond to the compression cases A-D indicated in Fig. 8a.

The amplitude swing retrieved spectral phases (Fig. 9, column 3, red curve) are compared to those obtained from the d-scan technique (Fig. 9, column 3, blue curve), where the second and third order phase coefficients are given inset for comparison (GDD and TOD of each pulse calculated from a third-order polynomial fit of the spectral phase). The average discrepancy between the two techniques in the GDD is <3% (excluding point B because of being close to GDD=0 fs^2), while for the TOD the average discrepancy is below 6% (note that the d-scan retrievals have their own error). Nevertheless, the impact of those differences on the retrieved pulse is acceptable, which is corroborated by the comparison of the temporal domain intensities.

The corresponding pulse intensities in the time domain are shown in Fig. 9, column 4, comparing again the amplitude swing (blue curve) and the d-scan (red curve) retrievals (intensity duration FWHM given inset for comparison). The agreement between both techniques is good, including cases with almost pure TOD (case B), as well as cases of TOD combined with a predominant positive (cases C and D) or negative GDD (case A), thus validating the amplitude swing method, so that this technique is able to cover broad ranges of pulse chirp.

In order to interpret the results, it is important to realize that the SHG is different for the 4 cases shown here. If observing the d-scan trace, the central wavelength of a pulse with TOD is shifted from bluer to redder wavelengths when adding positive GDD to the pulse. Therefore, the SHG of the pulse in position A is peaked at 396 nm and for position B in 399 nm (see the sections of the d-scan trace in Fig. 8a). This is the reason of having more signal at those wavelengths in the amplitude swing trace (Fig. 9(A1) and 9(B1), respectively). It is also seen that, in Fig. 9(B1), the trace is narrower because of having an almost pure TOD (case B), while in Fig. 9(A1) the positive TOD is combined with negative GDD. In the case of positions C and D, the peak is shifted to around 401 nm and 402 nm, while reducing its signal with respect to a contribution at 398 nm that increases when adding positive GDD (see sections of Fig. 8a). Those sections of the d-scan trace appear in the amplitude swing traces for angles θ=0, 90 and 180º, while for intermediate angles the SHG spectrum is modulated according to the spectral phase of the input pulse and the two replicas interference.

Notice that, compared to the simulations of Sections 2 and 3, in the experiments the MWP delay is different from the Fourier-limit FWHM of the pulse, and it introduces a different retardation for the central wavelength. This is not a requirement of the technique, so it stands to correctly reconstruct the pulses. Taking into account that the MWP operates as half-wave for 800.5 nm, for the case of dominating pure TOD (case B), the amplitude swing trace is sharp at 399 nm as seen in the simulations shown in Fig. 3 and 5. When adding positive GDD (case C) the trace presents a pair of holes at both sides of 400 nm for θ=45 and 135º, with orientation similar to the case in Fig. 2, column 4, indicating the presence of moderate positive chirp. Therefore, in a general case with an arbitrary MWP, apart from being able to retrieve the pulses, it may be possible to identify basic cases of pulse chirp, which may be used to optimize the pulse.

5. Conclusions

A new strategy for temporal pulse reconstruction is presented, consisting in the collection of the nonlinear spectra generated in a nonlinear medium by a pair of replicas of the unknown pulse with a given time delay while varying their relative amplitude. The analytical description of the technique for pulses presenting Gaussian shaped spectrum and quadratic spectral phase has been used for giving an intuition of the technique principles when it is scanned the amplitude balance between the replicas. Other cases (e.g., third-order spectral phases) have been numerically studied. The retrieval method here presented for the pulse reconstruction is based on the Levenberg-Marquardt optimization algorithm. It has been tested in the explored theoretical cases, obtaining good convergence and accurateness. The

technique has been validated experimentally by comparison with the pulse reconstructions of a stablished technique, observing good agreement at different spectral phase cases.

Therefore, the amplitude swing is a simple and robust inline technique, which can be implemented with common and inexpensive optical elements (e.g., wave-plates, optical polarizers). The in-line configuration of the interferometer (i.e., the multiorder wave-plate) confers the set-up stability, compactness and makes the beam alignment direct as it does not present beam recombination or moving beam-lines. In addition, the set-up could be easily adapted to cover a broad range of pulse durations (from few-cycle to several picosecond pulses) just by changing the waveplate thickness (by replacing the element itself or by using a varying thickness wave-plate made up, for example, by a pair of birefringent wedges), provided that the nonlinear medium shows correct phase matching.

Funding

Spanish Ministerio de Economía y Competitividad (MINECO) (FIS2017-87970-R, EQC2018-004117-P), Consejería de Educación, Junta de Castilla y León (SA287P18) and FEDER Funds, Fundación General de la Universidad de Salamanca (PC_TCUE18-20_020).

Disclosures

The authors declare no conflicts of interest.

References

1. I. A. Walmsley and C. Dorrer, "Characterization of ultrashort electromagnetic pulses," Adv. Opt. Photonics **1**, 308–437 (2009).
2. H. Timmers, Y. Kobayashi, K. F. Chang, M. Reduzzi, D. M. Neumark, and S. R. Leone, "Generating high-contrast, near single-cycle waveforms with third-order dispersion compensation," Opt. Lett. **42**, 811–814 (2017).
3. F. Silva, B. Alonso, W. Holgado, R. Romero, J. S. Román, E. C. Jarque, H. Koop, V. Pervak, H. Crespo, and Í. J. Sola, "Strategies for achieving intense single-cycle pulses with in-line post-compression setups," Opt. Lett. **43**, 337–340 (2018).
4. A. Wirth, M. T. Hassan, I. Grguras, J. Gagnon, A. Moulet, T. T. Luu, S. Pabst, R. Santra, Z. A. Alahmed, A. M. Azzeer, V. S. Yakovlev, V. Pervak, F. Krausz, and E. Goulielmakis, "Synthesized Light Transients," Science **334**, 195–200 (2011).
5. J. A. Armstrong, "Measurement of picosecond laser pulse widths," Appl. Phys. Lett. **10**, 16–18 (1967).
6. D. J. Kane and R. Trebino, "Characterisation of arbitrary femtosecond pulses using frequency-resolved optical gating," IEEE J. Quantum Electron. **29**, 571–579 (1993).
7. R. Trebino and D. J. Kane, "Using phase retrieval to measure the intensity and phase of ultrashort pulses: frequency-resolved optical gating," J. Opt. Soc. Am. A **10**, 1101–1111 (1993).
8. K. W. DeLong, B. Kohler, K. Wilson, D. N. Fittinghoff, and R. Trebino, "Pulse retrieval in frequency-resolved optical gating based on the method of generalized projections," Opt. Lett. **19**, 2152–2154 (1994).
9. C. Iaconis and I. A. Walmsley, "Spectral phase interferometry for direct electric-field reconstruction of ultrashort optical pulses," Opt. Lett. **23**, 792–794 (1998).
10. T. Oksenhendler, S. Coudreau, N. Forget, V. Crozatier, S. Grabielle, R. Herzog, O. Gobert, and D. Kaplan, "Self-referenced spectral interferometry," Appl. Phys. B-Lasers Opt. **99**, 7–12 (2010).
11. V. V. Lozovoy, I. Pastirk, and M. Dantus, "Multiphoton intrapulse interference IV Ultrashort laser pulse spectral phase characterization and compensation," Opt. Lett. **29**, 775–777 (2004).
12. B. Xu, J. M. Gunn, J. M. Dela Cruz, V. V. Lozovoy, and M. Dantus, "Quantitative investigation of the multiphoton intrapulse interference phase scan method for simultaneous phase measurement and compensation of femtosecond laser pulses," J. Opt. Soc. Am. B **23**, 750–759 (2006).
13. M. Miranda, T. Fordell, C. Arnold, A. L'Huillier, and H. Crespo, "Simultaneous compression and characterization of ultrashort laser pulses using chirped mirrors and glass wedges," Opt. Express **20**, 688–697 (2012).
14. M. Miranda, C. L. Arnold, T. Fordell, F. Silva, B. Alonso, R. Weigand, A. L'Huillier, and H. Crespo, "Characterization of broadband few-cycle laser pulses with the d-scan technique," Opt. Express **20**, 18732–18743 (2012).
15. M. Miranda, J. Penedones, C. Guo, A. Harth, M. Louisy, L. Neoričić, A. L'Huillier, and C. L. Arnold, "Fast iterative retrieval algorithm for ultrashort pulse characterization using dispersion scans," J. Opt. Soc. Am. B **34**, 190–197 (2017).
16. B. Alonso, Í. J. Sola, and H. Crespo, "Self-calibrating d-scan: Measuring ultrashort laser pulses on-target

using an arbitrary pulse compressor," Sci. Rep. **8**, 3264 (2018).
17. E. Escoto, A. Tajalli, T. Nagy, and G. Steinmeyer, "Advanced phase retrieval for dispersion scan: a comparative study," J. Opt. Soc. Am. B **35**, 8–19 (2018).
18. V. Loriot, G. Gitzinger, and N. Forget, "Self-referenced characterization of femtosecond laser pulses by chirp scan," Opt. Express **21**, 24879–24893 (2013).
19. C. Dorrer and F. Salin, "Characterization of spectral phase modulation by classical and polarization spectral interferometry," J. Opt. Soc. Am. B **15**, 2331–2337 (1998).
20. P. Schlup, J. Wilson, K. Hartinger, and R. A. Bartels, "Dispersion balancing of variable-delay monolithic pulse splitters," Appl. Opt. **46**, 5967–5973 (2007).
21. P. O'Shea, M. Kimmel, X. Gu, and R. Trebino, "Highly simplified device for ultrashort-pulse measurement," Opt. Lett. **26**, 932–934 (2001).
22. V. Wong and I. A. Walmsley, "Linear filter analysis of methods for ultrashort-pulse-shape measurements," J. Opt. Soc. Am. B **12**, 1491–1499 (1995).
23. G. Ghosh, "Dispersion-equation coefficients for the refractive index and birefringence of calcite and quartz crystals," Opt. Commun. **163**, 95–102 (1999).
24. B. Alonso and Í. Sola, "Measurement of Ultrashort Vector Pulses From Polarization Gates by In-Line, Single-Channel Spectral Interferometry," IEEE J. Sel. Top. Quantum Electron. **25**, 8900307 (2019).
25. F. Silva, M. Miranda, B. Alonso, J. Rauschenberger, V. Pervak, and H. Crespo, "Simultaneous compression, characterization and phase stabilization of GW-level 14 cycle VIS-NIR femtosecond pulses using a single dispersion-scan setup," Opt. Express **22**, 10181–10191 (2014).
26. B. Alonso, S. Torres-Peiró, R. Romero, P. T. Guerreiro, A. Almagro-Ruiz, H. Muñoz-Marco, P. Pérez-Millán, and H. Crespo, "Detection and elimination of pulse train instabilities in broadband fibre lasers using dispersion scan," Sci. Rep. **10**, 7242 (2020).
27. N. C. Geib, M. Zilk, T. Pertsch, and F. Eilenberger, "Common pulse retrieval algorithm: a fast and universal method to retrieve ultrashort pulses," Optica **6**, 495–505 (2019).
28. F. Silva, M. Miranda, and H. Crespo, "Measuring few-cycle laser pulses: A comparative study between dispersion-scan and FROG," in *2013 Conference on Lasers and Electro-Optics Europe and International Quantum Electronics Conference, CLEO/Europe-IQEC 2013* (Optical Society of America, 2013), p. CFIE_P_17.
29. M. Miranda, P. Rudawski, C. Guo, F. Silva, C. L. Arnold, T. Binhammer, H. Crespo, and A. L'Huillier, "Ultrashort laser pulse characterization from dispersion scans: a comparison with SPIDER," in *CLEO: 2013*, OSA Technical Digest (online), ed. (Optical Society of America, 2013), p. JTh2A.31.